In Situ TEM Characterization of Shear-Stress-Induced Interlayer Sliding in the Cross Section View of Molybdenum Disulfide

Juan Pablo Oviedo, Santosh KC, Ning Lu, Jinguo Wang, Kyeongjae Cho, Robert M. Wallace, and Moon J. Kim*

Materials Science and Engineering Department, The University of Texas at Dallas, 800 West Campbell Road, Richardson, Texas 75080, United States

ABSTRACT The experimental study of interlayer sliding at the nanoscale in layered solids has been limited thus far by the incapability of mechanical and imaging probes to simultaneously access sliding interfaces and overcome through mechanical stimulus the van der Waals and Coulombic interactions holding the layers in place. For this purpose, straightforward methods were developed to achieve interlayer sliding in molybdenum disulfide (MoS_2) while under observation within a transmission electron microscope. A method to manipulate, tear, and slide free-standing atomic layers of MoS_2 is demonstrated by electrostatically coupling it to an oxidized tungsten probe attached to a micromanipulator at a bias above ± 7 V. A first-principles model of a MoS_2 bilayer polarized by a normal electric field of 5 V/nm, emanating from the tip, demonstrates the appearance of a periodic negative sliding potential energy barrier when the layers slide into the out-of-registry stacking configuration, hinting at electrostatic gating as a means of modifying the interlayer tribology to facilitate shear exfoliation. A method to shear focused ion beam prepared MoS_2 cross section samples using a nanoindenter force sensor is also demonstrated, allowing both the observation and force measurement of its interlayer dynamics during shear-induced sliding. From this experiment, the zero normal load shear strength of MoS_2 can be directly obtained: 25.3 ± 0.6 MPa. These capabilities enable the site-specific mechanical testing of dry lubricant-based nanoelectromechanical devices and can lead to a better understanding of the atomic mechanisms from which the interlayer tribology of layered materials originates.

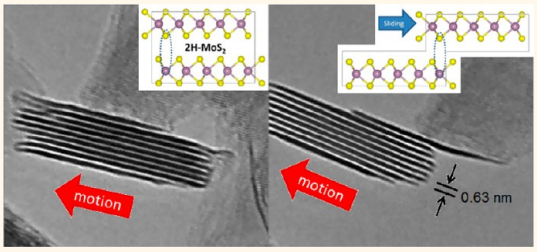

KEYWORDS: molybdenum disulfide · *in situ* TEM · nanotribology · interlayer sliding · shear strength

The lubricating properties of molybdenum disulfide, a common layered compound, have been the subject of study of tribology for decades.[1] These are derived from the low strength of its interplanar van der Waals bonds compared to the basal plane covalent bonds,[2,3] allowing layers within these planes to slide easily when shear stress is applied, a process known as "interlayer sliding". Studying this process at the macroscopic scale commonly involves measuring friction in a tribometer between MoS_2-coated sliding and/or rolling contact interfaces of minimal surface roughness, in order to make interlayer sliding the dominant friction process over adhesion and plowing.[4] Using this setup, it has been determined that molybdenum disulfide nanoflakes have better lubricating properties than microflakes, due to their ability to better penetrate and conform to the contact region.[5] It has also been demonstrated that the friction coefficient between interfaces lubricated with molybdenum disulfide decreases with increasing pressure.[4,6,7] In order to explain this effect, models of atomic friction between MoS_2 layers have been developed, which suggest that pressure has the effect of increasing the corrugation of the sliding potential energy surface of MoS_2, which arises from the Coulombic interaction between the negatively charged sulfur atoms on opposite sides of the layers.[2,8−10] Other experiments have focused on measuring the shear strength of molybdenum disulfide films in different environments. They have found that the shear strength varies from 0.7 to 1.1 MPa in ultrahigh vacuum or dry nitrogen to 4.9 MPa in high vacuum and 56 MPa in ambient air.[11]

* Address correspondence to moonkim@utdallas.edu.

Received for review October 23, 2014 and accepted December 12, 2014.

Published online December 12, 2014
10.1021/nn506052d

In comparison, there have been relatively few experimental studies focusing on the interlayer sliding process of molybdenum disulfide at the nanoscale, which would provide a direct correlation between the stacking configuration of the layers and the forces arising from their relative motion. One of the main reasons for this is the difficulty in applying proper shear stress to the interlayer interface of a single microscopic flake of a layered material using a probe, such as in friction force microscopy, which can result in out-of-plane elastic deformation, as opposed to sliding, when the probe-layer interactions are weaker than the interlayer interactions.[12] This problem was addressed by Liu *et al.*,[13] using a SiO_2 cap on highly oriented pyrolitic graphite mesas as a means to evenly transfer shear stress from a probe to the interlayer interface of graphite. This was also the first experiment to demonstrate its angle-dependent sliding anisotropy and the frictionless self-retraction of its sheared surfaces due to incommensurate contact, a phenomenon known as superlubricity, also predicted to occur in MoS_2.[14] The other reason lies in the technical difficulties associated with the observation of the interlayer sliding process in cross section view, only possible using transmission electron microscopy (TEM), which introduces further geometrical constraints to the lateral dimensions of the sample, requiring it to be electron transparent in order to resolve individual layers in motion. Great strides have been made using *in situ* transmission electron microscopy to observe the interlayer sliding process of layered materials, the most successful example being the recording of the telescoping motion of nested carbon nanotube shells.[15−17] In such systems, interlayer sliding occurs between an outer nanotube shell and an exposed nanotube core, which can be pulled out by a micromanipulator probe, analogous to a nanoscale linear bearing.[15] This simplifies the manipulation problem, as the system is constrained to move in one dimension and thus can be easily accessed by probes or force sensors while it is imaged with the electron beam. This method allowed to correlate for the first time the atomic defects observed in the nanotube lattice with the forces measured during its telescoping motion.[16] In comparison, applying shear stress *in situ* to a planar interface, such as a nanoflake or a cross section sample of a layered solid, remains a challenging nanomechanical procedure, as a protocol to achieve interlayer sliding within such systems has yet to be established.

In this work, two techniques for the characterization of interlayer sliding of MoS_2 flakes in cross section view are demonstrated using *in situ* transmission electron microscopy. One permits the accurate mechanical nanomanipulation of few-layer MoS_2 nanoflakes and sliding of monolayers in a controllable manner, by coupling them to a probe under electrostatic bias. The second technique allows measuring the forces involved in shearing a focused ion beam (FIB) prepared MoS_2 flake cross section sample as its structural changes are simultaneously observed.

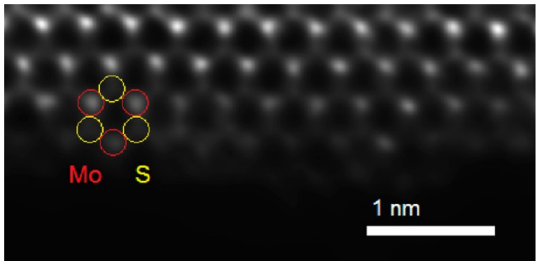

Figure 1. Plane-view MoS_2 flake edge. STEM-HAADF deconvoluted image of MoS_2 in the [001] zone axis orientation showing molybdenum and sulfur atoms in a hexagonal configuration, characteristic of the 2H structure, with high signal intensity positions corresponding to molybdenum and low signal intensity positions corresponding to sulfur.

RESULTS AND DISCUSSION

Structure of MoS_2 Flakes Used for *In Situ* Studies. In order to correlate the sliding properties of MoS_2 layers with their atomic structure, the determination of the phase of MoS_2 used is paramount. There are two known phases of MoS_2: trigonal prismatic (2H) and octahedral (1T).[18] The atomic structure of flakes obtained from bulk MoS_2 was determined by acquiring plane-view high-angle annular dark-field (HAADF) scanning transmission electron microscope (STEM) images (see Methods, high-resolution STEM-HAADF imaging of MoS_2), revealing the positions of molybdenum and sulfur atoms by their mass density contrast, arranged in a hexagonal configuration, as depicted in Figure 1, with Mo−S and Mo−Mo separations of ∼0.19 and ∼0.33 nm, respectively, coinciding with the structure of 2H-MoS_2.

Electrostatic Probe-Assisted Manipulation of MoS_2. The ability to manipulate monolayers of molybdenum disulfide *in situ* was recently demonstrated by Tang *et al.*,[19] using an ultrasharp (10 nm in diameter) tungsten probe to cleave atomic layers from MoS_2 by making contact with their outermost edge and pulling them back at an angle. An alternate route to manipulate flakes of molybdenum disulfide with a broader range of probe sizes (10−200 nm in diameter) was identified by attaching them to the surface of an etched tungsten probe with a thick (6−8 nm) native oxide layer at its tip at a high dc electrostatic bias (generally above ±7 V), independent of polarity (see Methods, *in situ* STM probing experiment). Using this electrostatic probe mounted on a piezoelectric manipulator inside the TEM, precise positioning control of molybdenum disulfide flakes could be achieved, with the freedom to apply mechanical force in any arbitrary normal or tangential direction to its tip. The strength of the coupling was adjusted by simply varying the electric field intensity through the probe bias, being sufficient to directly tear small nanoflake pieces of MoS_2 (generally between 10 and 50 nm in size) from

the edge of bulk flakes (Supporting Information Figures S1−S3). The limit of the force which could be applied through this means was imposed by the dielectric strength of the oxide on the tungsten tip, which would generally reach dielectric breakdown above ±40 V. One key feature of this effect was the equal attraction of MoS_2 nanoflakes to both the tip and bulk MoS_2 on opposite sides of the open circuit, suggesting that the charge distribution in these nanoflakes became polarized by the high electric field emitted by the tip. Based on the model created by Santos and Kaxiras,[20] who predicted the dielectric properties of MoS_2 polarized by a high external electric field applied perpendicular to the layers, the electric field magnitude necessary to observe this effect could be estimated within a 0.8 to 15 V/nm range for bilayer MoS_2 and lower for thicker flakes. Similar behavior was also previously described by the authors in bilayer graphene in a perpendicular electric field of 1 V/nm.[21] These values were confirmed by carrying out first-principles calculations based on density functional theory (DFT) (see Methods, first-principles calculations of electric field response and sliding energy barriers), modeling the charge distribution in the bilayer 2H-MoS_2 system under the effect of a perpendicular external electric field, obtaining significant electron accumulation and depletion at opposite faces of the bilayer system at a field magnitude of 5 V/nm (Supporting Information Figure S4). However, during its manipulation, MoS_2 was in direct contact with the tip, so substrate-induced polarization due to Fermi level pinning could also play a role in this effect.[22] Together, these models provide the theoretical basis to explain the bias-dependent strength of the tip-to-flake and flake-to-flake mechanical coupling interactions observed.

MoS_2 Monolayer *In Situ* Interlayer Sliding and Exfoliation Process. Using the extended manipulation capabilities of the oxidized tungsten probe at a +10 V dc bias, a 20 nm, nine layer MoS_2 nanoflake could be directly torn from a free-standing exfoliated flake and aligned in cross section view (Supporting Information movies 1−3). A line profile of the cross section of the flake verified that the top layer constituted a monolayer of MoS_2, with a thickness of 0.63 nm (Supporting Information Figure S5). An interlayer sliding process ensued, shown in Figure 2, following the sliding of the top layer of the nanoflake, held between the edges of two MoS_2 flakes submitted to the electrostatic field of the tip. Shearing force was applied by moving the tip in the left direction in discrete steps, while the top contact flake held the upper-layer static. The lateral force was transmitted to four of the nine layers in the stack in edge contact with the perpendicular leftmost flake (Figure 2c). Smooth sliding of the top monolayer could be seen as shearing progressed, from the initial position, to about half the monolayer's diameter (Figure 2a−e). Beyond this point, a side of the monolayer bent toward the edge of the flake as it slid, indicating that there was less contact area to keep this side taught (Figure 2f,g). Also, at this stage, the surface underneath the sliding monolayer became uneven and step-like due to the formation of a layer stacking defect, arising both from e-beam exposure (Supporting Information Figure S6) and stress in the lattice. At a sliding distance 2/3 of the monolayer's diameter (Figure 2h), the flake swelled and the bent side of the monolayer became free. Immediately after, the monolayer was exfoliated and became attached to the upper flake. An interlayer contact-area-dependent exfoliation threshold appeared to determine the point at which the monolayer was exfoliated. An incomplete relaxation of the interlayer shear stresses as well as vibration from the tip could have led to the premature exfoliation of the monolayer once the contact area was small enough to reach the interlayer shear strength of the material. However, the point at which the monolayer debonded was also the same point at which the upper-layer-holding flake did not overlap the bulk of the nanoflake. At this point, the monolayer area in contact with the nanoflake held itself purely through unscreened interlayer interactions. Therefore, the presence of the electric field emitted by the electrostatic probe could have also altered these interactions, leading to a premature exfoliation.

The force required to slide the monolayer can be described as $F(|E|,x) = F_{if}(|E|,x) + F_{see}(|E|,x)$. The first term is the interlayer friction force, $F_{if}(|E|,x) = \tau_f(|E|)A(x)$, where $\tau_f(|E|)$ is the shear strength of MoS_2 polarized in a high electric field of norm $|E|$, and $A(x)$ represents the decreasing interlayer contact area with increasing lateral displacement x of the probe. The second term, $F_{see}(|E|)$, represents the cohesive force originating from surface energy and edge effects, $F_{see}(|E|) = -2\gamma(|E|)(dA(x)/dx)$, where $\gamma(|E|)$ is the surface energy of MoS_2 in a high electric field environment. This electric field dependence was suggested by the model developed by Santos and Kaxiras,[20] which showed that a high electric field could decrease the interlayer binding energy of MoS_2, also confirmed in our model (Supporting Information Figure S7), thus making it more prone to exfoliation. As the monolayer slid, new surface area $A^*(x) = 2(A_i - A(x))$ was created, where A_i is the initial interlayer contact area, 160 nm^2. The excess surface free energy achieved after the complete exfoliation of the monolayer is $U = 2\gamma(|E|)A_i$, where $\gamma(0)$, the surface energy of MoS_2 at zero external electric field, has been estimated from liquid exfoliation experiments as 7×10^{-2} J/m^2,[23] creating ~140 eV of excess surface free energy during the exfoliation process, though values for $\gamma(|E|)$ in a high electric field environment could be lower due to the lower binding energy argument.

In order to evaluate the impact of the electric field created by the tip on the sliding process, its effect was modeled using first-principles calculations (based on density functional theory) of the interlayer sliding

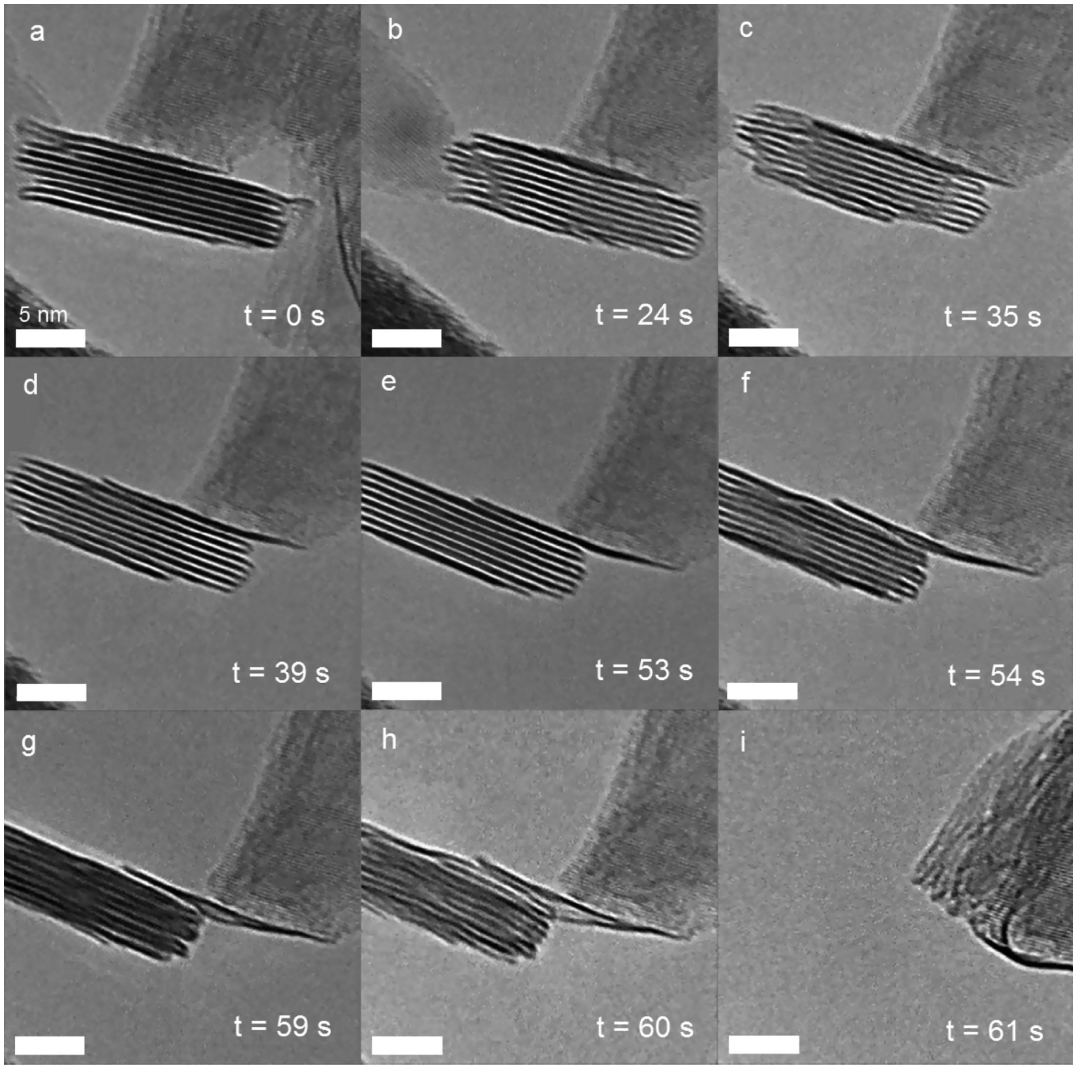

Figure 2. Video frame captures of a molybdenum disulfide monolayer sliding process. (a−i) A nine layer nanoflake is seen in the middle, held between the edges of two MoS_2 flakes. Stepwise sideways motion of the oxidized tungsten tip at a bias of +10 V led to shearing of the top monolayer of the nanoflake. See Supporting Information movie 3.

energy of bilayer 2H-MoS_2 with a contact area of 2.11 nm^2. The bottom layer was fixed, while the top layer was moved horizontally in incremental steps and relaxed, starting from the thermodynamically stable A−B stacking sequence. Nonidentical periodic pathways for interlayer sliding were explored (Supporting Information Figures S8 and S9), and the most energetically favorable straight path was identified in the [100] direction, with the lowest energy barrier without an external electric field applied being 0.14 eV (Figure 3). By applying a 5 V/nm electric field normal to the basal plane of 2H-MoS_2, previously confirmed sufficient to induce its polarization, the initial barrier on this path is raised to 0.2 eV. Past the first barrier, the sliding energy becomes negative (−0.25 eV), in contrast with the positive value at this position in the absence of an external electric field (0.14 eV), creating a bound state requiring 0.45 eV to resume sliding. This is a direct consequence of polarization affecting the Coulomb

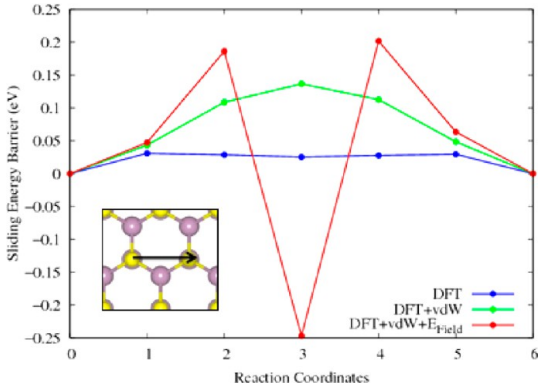

Figure 3. Sliding energy barriers for 2H-MoS_2 layers in the [100] direction. The green line shows the dispersion-corrected (DFT + van der Waals) energy barriers, and the blue line shows the DFT energy barriers without the correction. The red line shows the dispersion-corrected energy barriers with an external electric field of 5 V/nm applied perpendicular to the basal plane of the layers.

interaction, which is modulated by the position of the terminal atoms of the top and bottom layer and the charge density distribution. However, this bound state would seem to imply that the layers are more strongly bound at an intermediate stacking position, a counterintuitive result. Blumberg *et al.*[10] showed the equivalence between the geometrical stacking of MoS_2 layers and their sliding potential energy surface through an interlayer registry index, proving that points of ideal stacking corresponded to points of sliding potential energy minima, while points of nonideal stacking led to maxima, albeit without an external electric field. Based on their model, our interpretation of the negative sliding energy barrier when the electric field is applied is the following: After overcoming the 0.2 eV positive barrier, existing due to the lack of registry between the layers, it becomes energetically favorable for the top layer to position itself on the location of maximum separation between the layers along the path and remain there due to the negative potential energy value. This is consistent with the expected decrease in energy with increasing separation distance under a high perpendicular electric field.[20] However, with sliding impeded, this scenario would be favorable for the vertical separation of the top layer if the energy required for this process were smaller than that required to resume sliding. Our *in situ* TEM observations are consistent with this model. As depicted in Figure 2h,i, when the upper-layer-holding flake moves away from the bulk of the nanoflake, the free-standing side of the monolayer finds itself locked in its current position by a higher sliding energy barrier than before (the 0.2 eV barrier in our model), preventing further sliding, and by forcing it to keep shearing, the interlayer separation increases (the swelling effect) until exfoliation happens. Thus, the sliding path required for the exfoliation of a monolayer could be significantly shortened using a high electric field since a sliding distance of only half a unit cell of MoS_2 would be required to separate the layers enough for electric-field-induced vertical exfoliation to take over. Coincidentally, the mechanical separation of monolayers from layered powders through interlayer sliding in liquid dispersion, also known as "shear exfoliation", has recently proven to be a scalable approach for the industrial production of 2D materials.[23−25] However, currently, the technique can only achieve an exfoliation yield of less than 1%. The facile shear exfoliation of MoS_2 under a high electric field environment could have potential applications in increasing the yield and efficiency of this process by applying an electric field at strategic high shear zones within a high shear mixer head used to exfoliate the flakes, which would bring down the cost of scaling this process by cutting down the energy used to separate a given amount of layered material.

Microforce Shearing Test Experimental Setup. In order to provide an estimate of the shear stresses occurring during interlayer sliding, an accurate determination of the interlayer shear strength of a single flake of MoS_2 is required. Thus, both the force and the interlayer contact area at the point of shear exfoliation are needed. A mechanical test was designed which would allow shearing a cross section sample of a MoS_2 flake within the TEM and detect the shear force applied to it using a nanoindenter force sensor (see Methods, *in situ* microforce mechanical testing). By carrying out the mechanical test *in situ*, the contact point which would apply the shear force to the flake could be precisely aligned, and each point in the force *versus* distance plot could also be correlated with the process of interlayer sliding in cross section view. The cross section sample consisted of a 50 nm thick flake of MoS_2 held between a 3.5 μm thick FIB deposited platinum cap and a 90 nm SiO_2 layer on a Si(100) substrate attached with FIB deposited platinum to a modified Cu lift-out grid, which could be freely moved by fixing it to the same nanomanipulator used for the *in situ* monolayer sliding experiment (Figure 4a). An electron transparent lamella was also created at the edge of this sample, by FIB milling, to track the position of the MoS_2 layers relative to their substrate (Figure 4b). Before loading the sample in the TEM, it was prealigned with the basal plane [120] crystallographic direction of MoS_2 approximately parallel to the nanoindenter diamond tip axis. This orientation was obtained from the symmetry of the parent flake (Supporting Information Figure S10) and was selected to favor measuring the interlayer friction forces of the material in commensurate contact throughout the test, avoiding structural superlubricity by incommensurate contact at a misfit angle.[9,14] Also, according to our simulation (Supporting Information Figure S9), this path would yield the highest resistance to sliding, giving an upper bound shear stress to initiate interlayer sliding in MoS_2. A 3D schematic of the sample is provided (Supporting Information Figure S11).

***In Situ* Mechanical Shearing Test of a MoS_2 Flake Cross Section Sample.** The MoS_2 cross section sample was programmed to move toward the static diamond indenter probe for a set distance and return to its starting position afterward, while applying force on the side of the Pt cap to create shear stress, as depicted in Figure 4a. At a distance of 630 nm from the initial position, shearing was detected, both on the live image from the TEM CCD camera and in the force *versus* distance plot (Figure 4c), inferred by the sudden disappearance of the lower half of the sample (Figure 4d,e) and a simultaneous drop in the force value, happening faster than the minimum time recording step, 0.134 s. The force at the point of shear, $F = 498.8 \pm 1.6\ \mu$N, was determined through a simple linear regression of the final portion of the graph, with a standard error of the estimate calculated as $\sigma_{est} = ((\Sigma(F[d] - F'[d]^2)/(N - 2)))^{1/2}$, where F is the measured force, F' is the estimated force, d is the distance, and N is the number of data points ($N = 129$). Further confirmation of shearing occurred

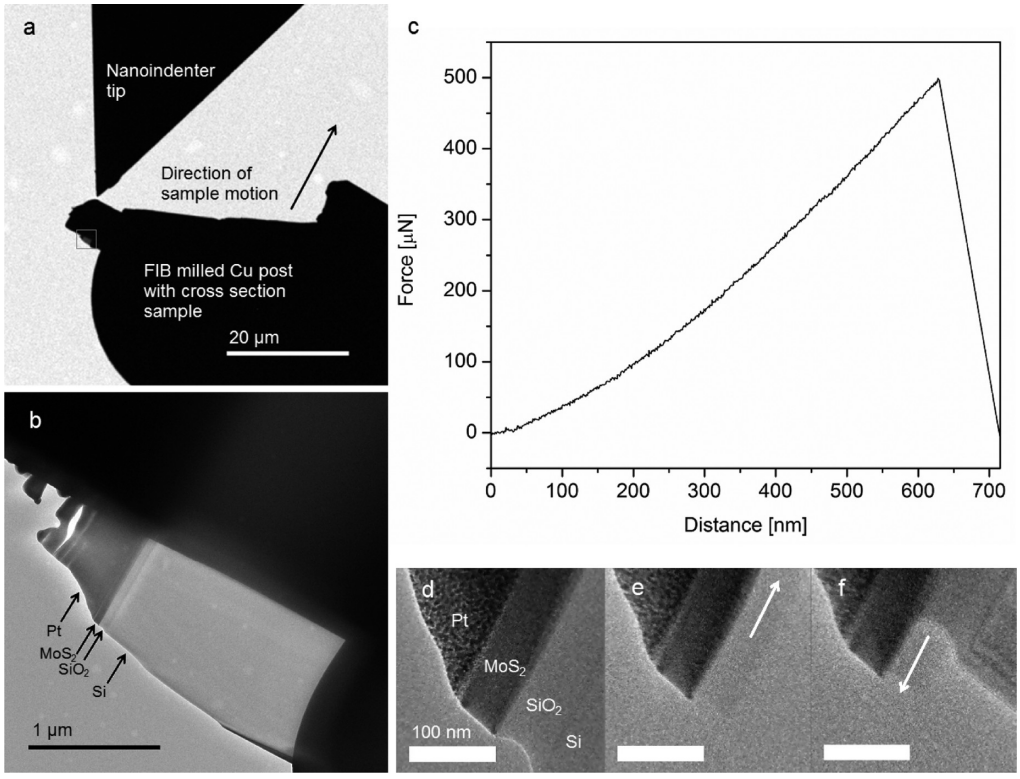

Figure 4. ***In situ*** **mechanical shearing test. (a) Low-magnification TEM image of the nanoindenter tip position relative to the cross section test sample on the Cu post of the modified lift-out grid. The gray square represents the location of the electron transparent lamella. (b) TEM image of the MoS_2 cross section sample seen through the lamella before the mechanical test. (c) Force** ***versus*** **distance plot recorded as the sample moved toward the static indenter tip. (d–f) Video frame captures of the edge of the lamella as the force was applied, before (d), during (e), and after shearing (f). The arrows represent the direction of motion of the lower half of the sample controlled by the nanomanipulator throughout the experiment. See Supporting Information movies 4 and 5.**

once the sample moved back to its original position, observing a shift in the alignment of the sheared halves of the lamella (Figure 4f). After the sample returned to its starting position, a fast "clapping" oscillation of its sheared top half was observed, as it was held by the indenter tip and the short-range forces between it and its bottom half (Supporting Information movie 6), proving that they had been separated. Upon closer examination of the lower half of the sample, a continuous monolayer of molybdenum disulfide was distinguished on top of the intact SiO_2 layer, with sparse discontinuous regions, 20–40 nm in length, of 2–6 layers (Figure 5a). No amorphous or damaged MoS_2 was seen on the surface of the SiO_2 layer. Thus, the failure mechanism was identified as a near interface cohesion-type fracture of MoS_2 with an in-plane shear failure mode, attributable to the interlayer sliding of its basal planes. The force value measured at the point of shearing could then be identified as the interlayer static friction force of MoS_2. After the experiment, a precise measurement of the sheared area was possible through SEM analysis by acquiring images of the sample at a normal orientation to the sheared surface (Figure 5b). The area obtained was $A = 19.7 \pm 0.5\ \mu m^2$, using a scale bar precision of ±50 nm, obtained from a calibration standard. The force and the area measured corresponded only to the sample's preparation conditions. Therefore, the only meaningful value was the shear strength derived from both.

The shear strength in the [120] direction of the MoS_2 cross section sample from the microforce shearing experiment in the vacuum environment of the TEM column (2×10^{-5} Pa) was calculated as $\tau_f = F/A = 25.3 \pm 0.6$ MPa. This result matched favorably with the macroscopic shear strength of sputter deposited MoS_2 films in air at zero Hertzian contact pressure estimated by Singer *et al.*,[6] 24.8 ± 0.5 MPa, with a 2% relative error due to the negligible effect of the normal contact pressure on the shear strength (Supporting Information Figures S12 and S13) and the fact that the flake had been previously exposed to air (thus adsorbing air molecules). This value also fell within the range of shear strengths of MoS_2 reported thus far (0.7–80 MPa).[4,7,11] Factors that were beyond our control during this experiment included the small-angle misalignment of the applied shear force, the influence of electron beam charging on the force-sensing instrumentation (minimized during calibration), the limitations of our setup compared to a standard shear strength testing apparatus,[26] causing an asymmetric shear stress distribution in the sample (Supporting Information Figures S12, S14), and the contribution to the shear strength coming from the amorphized area

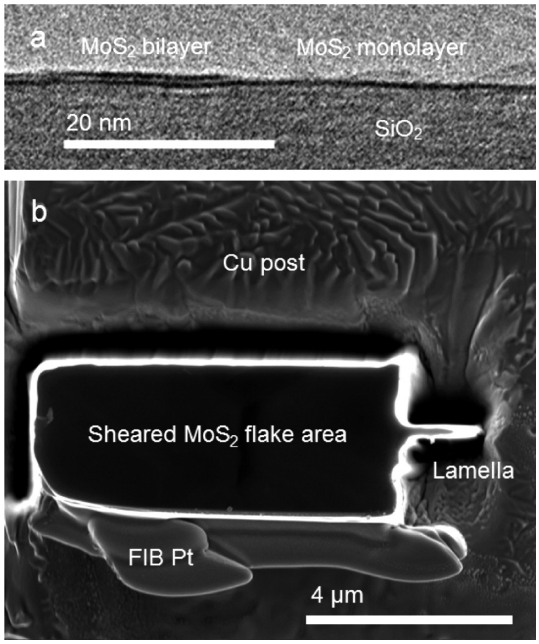

Figure 5. Sheared surface of the FIB cross section MoS_2 sample. (a) HRTEM cross section image of a continuous monolayer and an isolated bilayer of MoS_2 on the sheared SiO_2 surface of the electron transparent lamella. (b) Plane-view SEM image of the sheared surface after exfoliation. Three grain boundaries with the same crystal symmetry as the sheared flake (Supporting Information Figure S9) can be observed on the SiO_2 substrate.

at the perimeter of the FIB defined cross section sample, in this case with an average amorphization depth of 10 nm (Supporting Information Figures S15 and S16) accounting for 0.1% of the sheared area, with distinct mechanical shearing properties from pristine MoS_2. The high concentration of defects in this area could pin the adjacent layers, preventing their sliding and leading instead to their tearing (covalent bond breaking), as seen at the edges of the sample in Figure 5b, accounting for the discontinuous multilayer fragments observed (Figure 5a). The force required to reach the in-plane yield strength of these fragments can introduce artifacts in the measurement, such as obtaining a higher interlayer friction force value. This systematic error can be reduced by FIB milling the perimeter of the sample at lower ion beam currents and energies to minimize its damage. Nonetheless, the advantages of the *in situ* microforce shearing procedure, compared to previous macroscopic methods requiring a normal load to shear the interlayer interface, can be found in its straightforward approach to obtain the interlayer zero load shear strength of a layered material without further extrapolation from a series of pressure-dependent friction force measurements, and the fact that a crystallographic direction can be referenced to it, as opposed to a rotationally averaged value. The knowledge of this parameter can play a key role in the reliability of vertical heterojunctions of 2D materials, such as transition metal dichalcogenides, when subjected to shear strain in flexible and stretchable electronics.[27,28] Site-specific testing of mechanical sliding contact surfaces in nanoelectromechanical systems (NEMS) relying on van der Waals solids as a means of dry lubrication could also be realized by this technique, allowing the detection of interfacial atomic defects or intercalants hindering the device's operation by observation and *in situ* testing of FIB prepared cross section samples. As more sensitive instrumentation is developed, this method could also enable the correlation of interlayer atomic stacking positions within sliding layered solids with their respective dynamic friction force values, aiding in the development of more complete models of tribology in these materials.

CONCLUSIONS

Two approaches have been demonstrated to achieve interlayer sliding in 2H-MoS_2 samples under TEM examination in cross section view. The first method, suitable for free-standing flake samples, relies on the polarization of molybdenum disulfide under the electrostatic field of an etched and oxidized tungsten tip at a ± 7 V bias or above, to create a mechanically strong, yet tunable contact between them. This interaction has been demonstrated to be strong enough to break both covalent and van der Waals bonds in MoS_2, being capable of tearing it into a nanoflake morphology and shearing it down to a single monolayer. A MoS_2 monolayer sliding process was demonstrated *in situ* and modeled using first-principles simulations under a 5 V/nm electric field in the [100] direction, exhibiting a negative sliding barrier at the stacking configuration of largest interlayer separation deemed favorable for exfoliation. In addition, a FIB prepared MoS_2 flake cross section TEM sample was tested under shear stress *in situ* up to its mechanical failure point, and the empirical value for its shear strength at near zero normal pressure in the [120] direction was determined as 25.3 ± 0.6 MPa, in agreement with previous values. The techniques demonstrated in this work can be used for the industrial optimization of shear exfoliation of MoS_2 and similar 2D materials in liquid for the site-specific study of the mechanical reliability of heterojunctions and failure analysis of NEMS devices based on these materials and as a means to understand the atomic mechanisms giving rise to their lubricating properties.

METHODS

High-Resolution STEM-HAADF Imaging of MoS_2. Bulk MoS_2 (Ward's Science) was exfoliated using Scotch tape. The tape was pressed with clamps against a tungsten aperture TEM grid, and free-standing flakes were deposited on it, which were then rinsed with isopropyl alcohol to remove contamination from the tape.

A JEOL JEM-ARM 200F equipped with a Cs probe corrector was used to acquire plane-view STEM-HAADF images of this sample at 80 kV. In order to reduce the noise levels and to improve the accuracy of the image analysis, a probe deconvolution algorithm based on maximum entropy methods (DeConvHAADF-HREM Research Inc.) was applied to the images to remove the contribution of the tails of the focused electron probe to the column intensity.

***In Situ* STM Probing Experiment.** Bulk MoS_2 (Ward's Science) was exfoliated using Scotch tape. The tape was pressed with clamps against the tip of a flattened Au wire and peeled off to make a sample of free-standing multilayer flakes (Supporting Information Figure S1), which were then rinsed with isopropyl alcohol. The sample was then loaded on a Nanofactory Instruments AB STM holder along with a tungsten probe, etched from recrystallized tungtsten wire[29] (see Supporting Information Methods: STM tip etching), exposed to air for 2 weeks to leave a 6−8 nm thick native oxide layer, to be used as an electrostatic manipulator. Inside the TEM, the oxidized tip was approached at 0 V to a piece of few-layer MoS_2. Once contact was made, the bias on the Au wire was raised until ±10 V was reached without oxide breakdown, confirming the integrity of the dielectric film. Polarity did not matter. This value was chosen given the empirical observation of oxide breakdown at >±40 V. At this high bias, MoS_2 became electrostatically attached to the tip and to other flakes in series (see Supporting Information Methods: Electrostatic probe manipulation test). The tip was then used to tear small pieces of molybdenum disulfide from the bulk, align them in cross section (Supporting Informaiton Figures S2 and S3) and shear them (Supporting Information movies 1−3). A JEOL 2100F TEM at 200 kV was used to acquire images and video recordings.

***In Situ* Microforce Mechanical Testing.** Flakes of MoS_2 (Ward's Science) were first exfoliated from bulk pieces on 90 nm SiO_2 on Si substrates and cleaned with isopropyl alcohol. Then, flakes with crystallographic alignment between their principal crystallographic directions and the ⟨110⟩ directions of the underlying Si(100) substrate were sought after for HRTEM imaging. Focused ion beam cross section samples were made through FIB platinum bar deposition and the lift-out process[30] (Supporting Information Figure S9). A modified lift-out grid was used (see Supporting Information Methods: Custom lift-out grid preparation for side indentation), which allowed side access to the sample to a diamond indenter probe attached to a microforce sensor within a nanoindentation holder (Nanofactory Instruments AB). The sample was then mounted on a piezoelectric manipulator, manually aligned to the approximate Si [110] zone axis orientation, and loaded in the TEM. Once the sample was positioned with the indenter in side contact with the platinum bar, a 900 nm displacement was programmed for the sample to move toward the indenter at a rate of 10 nm/s. Force *versus* distance and force *versus* time plots were recorded during the experiment through the Nanofactory software. Images and video were recorded in a JEOL 2100F TEM at 200 kV. Supporting Information movie 6 was recorded with a cellphone camera fixed on the TEM viewing screen. SEM images were acquired in a FEI Nova Nanolab 200 Dualbeam at 5 kV, 1.6 nA.

First-Principles Calculations of Electric Field Response and Sliding Energy Barriers. First-principles calculations based on density functional theory were carried out using VASP code,[31−34] and the exchange correlation was represented by the generalized gradient approximation functional.[35,36] The atomic positions were optimized using the conjugate gradient scheme until the force convergence reached 0.01 eV/Å. Bilayer MoS_2 was simulated with a vacuum thickness of 10 Å to avoid spurious interaction between the images. The cut-off energy was 500 eV, and the Γ centered K-meshs of $6 \times 6 \times 1$ and $12 \times 12 \times 1$ were used for structure relaxation and self-consistence field calculations, respectively. The periodic sawtooth-like potential was applied perpendicular to the layers to simulate the external electric field. The dipole correction implemented in VASP was used. The sliding barrier for monolayers was estimated using the nudged elastic band method,[37] where several intermediate images were created for sliding of the top layer and each image was allowed to relax until the maximum residual force was less than 0.01 eV/Å. The van der Waals correction was implemented using the DFT-D2 method of Grimme.[38]

Conflict of Interest: The authors declare no competing financial interest.

Acknowledgment. This work was supported in part by the Center for Low Energy Systems Technology (LEAST), one of six centers of STARnet, a Semiconductor Research Corporation program sponsored by MARCO and DARPA. This work was supported in part by the South West Academy of Nanoelectronics (SWAN), a Center sponsored by the SRC Nanoelectronics Research Initiative and the National Institute of Standards and Technology. All calculations were performed using the computational resources of the Texas Advanced Computer Center (TACC) at the University of Texas at Austin. We acknowledge the support of the Mexican National Council for Science and Technology (CONACYT, 312723), through its CONACYT-UTD Program. J.P.O. performed the *in situ* TEM experiments and analyzed the data. N.L. obtained the STEM-HAADF images. S.K. carried out the DFT-based first-principles simulations. J.P.O. and S.K. co-wrote the paper. J.W., K.C., R.M.W., and M.J.K. supervised and oversaw the project. All authors discussed the results and added their comments to the manuscript.

Supporting Information Available: Supplementary figures and methods are provided detailing the *in situ* TEM experiments and DFT simulations, as well as a description of the tip etching process, sample preparation procedures, and finite element simulations of the mechanical response of the FIB prepared MoS_2 cross section test sample. Supplementary movies 1−3 demonstrate the alignment procedure of the MoS_2 nanoflake in cross section view and the interlayer sliding and exfoliation process of its top monolayer. Supplementary movies 4 and 5 show the process of shearing the FIB prepared MoS_2 cross section sample. Supplementary movie 6 shows in real time the oscillation frequency of the sheared top half of the FIB prepared MoS_2 cross section sample. This material is available free of charge *via* the Internet at http://pubs.acs.org.

REFERENCES AND NOTES

1. Winer, W. O. Molybdenum Disulfide as a Lubricant: A Review of the Fundamental Knowledge. *Wear* **1967**, *10*, 422–452.
2. Levita, G.; Cavaleiro, A.; Molinari, E.; Polcar, T.; Righi, M. C. Sliding Properties of MoS_2 Layers: Load and Interlayer Orientation Effects. *J. Phys. Chem. C* **2014**, *118*, 13809–13816.
3. Martin, J. M.; Pascal, H.; Donnet, C.; Le Mogne, T.; Loubet, J. L.; Epicier, T. Superlubricity of MoS_2: Crystal Orientation Mechanisms. *Surf. Coat. Technol.* **1994**, *68−69*, 427–432.
4. Grosseau-Poussard, J. L.; Moine, P.; Brendle, M. Shear Strength Measurements of Parallel MoS_x Thin Films. *Thin Solid Films* **1997**, *307*, 163–168.
5. Hu, K.; Cai, Y.; Hu, X.; Xu, Y. Synergistic Lubrication of MoS_2 Particles with Different Morphologies in Liquid Paraffin. *Ind. Lubr. Tribol.* **2013**, *65*, 143–149.
6. Singer, I. L.; Bolster, R. N.; Wegand, J.; Fayeulle, S.; Stupp, B. C. Hertzian Stress Contribution to Low Friction Behavior of Thin MoS_2 Coatings. *Appl. Phys. Lett.* **1990**, *57*, 995–997.
7. Briscoe, B. J.; Smith, A. C. The Interfacial Shear Strength of Molybdenum Disulfide and Graphite Films. *ASLE Trans.* **1982**, *25*, 349–354.
8. Onodera, T.; Morita, Y.; Suzuki, A.; Koyama, M.; Tsuboi, H.; Hatakeyama, N.; Endou, A.; Takaba, H.; Kubo, M.; Dassenoy, F.; *et al.* A Computational Chemistry Study on Friction of h-MoS_2. Part I. Mechanism of Single Sheet Lubrication. *J. Phys. Chem. B* **2009**, *113*, 16526–16536.
9. Onodera, T.; Morita, Y.; Nagumo, R.; Miura, R.; Suzuki, A.; Tsuboi, H.; Hatakeyama, N.; Endou, A.; Takaba, H.; Dassenoy, F.; *et al.* A Computational Chemistry Study on Friction of h-MoS_2. Part II. Friction Anisotropy. *J. Phys. Chem. B* **2010**, *114*, 15832–15838.
10. Blumberg, A.; Keshet, U.; Zaltsman, I.; Hod, O. Interlayer Registry To Determine the Sliding Potential of Layered

Metal Dichalcogenides: The Case of 2H-MoS_2. *J. Phys. Chem. Lett.* **2012**, *3*, 1936–1940.
11. Donnet, C.; Martin, J. M.; Le Mogne, T.; Belin, M. Super-low Friction of MoS_2 Coatings in Various Environments. *Tribol. Int.* **1996**, *29*, 123–128.
12. Lee, C.; Li, Q.; Kalb, W.; Liu, X.-Z.; Berger, H.; Carpick, R. W.; Hone, J. Frictional Characteristics of Atomically Thin Sheets. *Science* **2010**, *328*, 76–80.
13. Liu, Ze.; Yang, J.; Grey, F.; Liu, J. Z.; Liu, Y.; Wang, Y.; Yang, Y.; Cheng, Y.; Zheng, Q. Observation of Microscale Superlubricity in Graphite. *Phys. Rev. Lett.* **2012**, *108*, 205503.
14. Martin, J. M.; Pascal, H.; Donnet, C.; Le Mogne, T.; Loubet, J. L.; Epicier, T. Superlubricity of MoS_2: Crystal Orientation Mechanisms. *Surf. Coat. Technol.* **1994**, *68*−*69*, 427–432.
15. Cumings, J.; Zettl, A. Low-Friction Nanoscale Linear Bearing Realized from Multiwall Carbon Nanotubes. *Science* **2000**, *289*, 602–604.
16. Kis, A.; Jensen, K.; Aloni, S.; Mickelson, W.; Zettl, A. Interlayer Forces and Ultralow Sliding Friction in Multiwalled Carbon Nanotubes. *Phys. Rev. Lett.* **2006**, *97*, 025501.
17. Kuzumaki, T.; Mitsuda, Y. Characterization of Carbon Nanotubes by Nanoprobe Manipulation in Transmission Electron Microscope. *Diamond Relat. Mater.* **2008**, *17*, 615–619.
18. Lin, Y.-C.; Dumcenco, D. O.; Huang, Y.-S.; Suenaga, K. Atomic Mechanism of the Semiconducting-to-Metallic Phase Transition in Single-Layered MoS_2. *Nat. Nanotechnol.* **2014**, *9*, 391–396.
19. Tang, D.-M.; Kvashnin, D. G.; Najmaei, S.; Bando, Y.; Kimoto, K.; Koskinen, P.; Ajayan, P. M.; Yakobson, B. I.; Sorokin, P. B.; Lou, J.; *et al.* Nanomechanical Cleavage of Molybdenum Disulphide Atomic Layers. *Nat. Commun.* **2014**, *5*, 4631.
20. Santos, E. J. G.; Kaxiras, E. Electrically Driven Tuning of the Dielectric Constant in MoS_2 Layers. *ACS Nano* **2013**, *7*, 10741–10746.
21. Santos, E. J. G.; Kaxiras, E. Electric-Field Dependence of the Effective Dielectric Constant in Graphene. *Nano Lett.* **2013**, *13*, 898–902.
22. Chen, W.; Santos, E. J. G.; Zhu, W.; Kaxiras, E.; Zhang, Z. Tuning the Electronic and Chemical Properties of Monolayer MoS_2 Adsorbed on Transition Metal Substrates. *Nano Lett.* **2013**, *13*, 509–514.
23. Cunningham, G.; Lotya, M.; Cucinotta, C. S.; Sanvito, S.; Bergin, S. D.; Menzel, R.; Shaffer, M. S. P.; Coleman, J. N. Solvent Exfoliation of Transition Metal Dichalcogenides: Dispersibility of Exfoliated Nanosheets Varies Only Weakly between Compounds. *ACS Nano* **2012**, *6*, 3468–3480.
24. Paton, K. R.; Varrla, E.; Backes, C.; Smith, R. J.; Khan, U.; O'Neill, A.; Boland, C.; Lotya, M.; Istrate, O. M.; King, P.; *et al.* Scalable Production of Large Quantities of Defect-Free Few-Layer Graphene by Shear Exfoliation in Liquids. *Nat. Mater.* **2014**, *13*, 624–630.
25. Nicolosi, V.; Chhowalla, M.; Kanatzidis, M. G.; Strano, M. S.; Coleman, J. N. Liquid Exfoliation of Layered Materials. *Science* **2013**, *340*, 1226419.
26. ASTM Standard F1362. *Standard Test Method for Shear Strength and Shear Modulus of Aerospace Glazing Interlayer Materials*; ASTM International: West Conshohocken, PA, 2013; DOI: 10.1520/F1362, www.astm.org.
27. Roy, T.; Tosun, M.; Kang, J. S.; Sachid, A. B.; Desai, S. B.; Hettick, M.; Hu, C. C.; Javey, A. Field-Effect Transistors Built from All Two-Dimensional Material Components. *ACS Nano* **2014**, *8*, 6259–6264.
28. Pu, J.; Zhang, Y.; Wada, Y.; Tse-Wei Wang, J.; Li, L.-J.; Iwasa, Y.; Takenobu, T. Fabrication of Stretchable MoS_2 Thin-Film Transistors Using Elastic Ion-Gel Gate Dielectrics. *Appl. Phys. Lett.* **2013**, *103*, 023505.
29. Greiner, M.; Kruse, P. Recrystallization of Tungsten Wire for Fabrication of Sharp and Stable Nanoprobe and Field-Emitter Tips. *Rev. Sci. Instrum.* **2007**, *78*, 026104.
30. Giannuzzi, L. A.; Kempshall, B. W.; Schwarz, S. M.; Lomness, J. K.; Prenitzer, B. I.; Stevie, F. A. FIB Lift-Out Specimen Preparation Techniques: *Ex-Situ* and *In-Situ* Methods. In *Introduction to Focused Ion Beams: Instrumentation, Theory, Techniques and Practice*; Giannuzzi, L. A., Stevie, F. A., Eds.; Springer: New York, 2005; pp 201−228.
31. Kresse, G.; Furthmüller, J. Efficiency of *Ab-Initio* Total Energy Calculations for Metals and Semiconductors Using a Plane-Wave Basis Set. *Comput. Mater. Sci.* **1996**, *6*, 15–50.
32. Parr, R. G. Yang, W. *Density-Functional Theory of Atoms and Molecules*; Oxford University Press: New York, 1989.
33. Kohn, W.; Sham, L. J. Self-Consistent Equations Including Exchange and Correlation Effects. *Phys. Rev.* **1965**, *140*, A1133–A1138.
34. Blöchl, P. E. Projector Augmented-Wave Method. *Phys. Rev. B* **1994**, *50*, 17953–17979.
35. Kresse, G.; Hafner, J. *Ab Initio* Molecular Dynamics for Liquid Metals. *Phys. Rev. B* **1993**, *47*, 558–561.
36. Kresse, G.; Furthmüller, J. Efficient Iterative Schemes for *Ab Initio* Total-Energy Calculations Using a Plane-Wave Basis Set. *Phys. Rev. B* **1996**, *54*, 11169–11186.
37. Jonsson, H.; Mills, G.; Jacobsen, K. W. Nudged Elastic Band Method for Finding Minimum Energy Paths of Transitions. In *Classical and Quantum Dynamics in Condensed Phase Simulations*; Berne, B. J., Cicotti, G., Coker, D. F., Eds.; World Scientific: Singapore, 1998; pp 385−404.
38. Grimme, S. Semiempirical GGA-Type Density Functional Constructed with a Long-Range Dispersion Correction. *J. Comput. Chem.* **2006**, *27*, 1787–1799.